# Universiteit Antwerpen

## This item is the archived peer-reviewed author-version of:

Enhanced biomedical heat-triggered carriers via nanomagnetism tuning in ferrite-based nanoparticles

# Enhanced biomedical heat-triggered carriers via nanomagnetism tuning in ferrite-based nanoparticles

M. Angelakeris[a, b, ,] , Zi-An Li[b], M. Hilgendorff[b, 1], K. Simeonidis[a], D. Sakellari[a], M. Filippousi[c], H. Tian[c], G. Van Tendeloo[c], M. Spasova[b], M. Acet[b], M. Farle[b]

[a] Department of Physics, Aristotle University of Thessaloniki, 54124 Greece

[b] Fakultät für Physik and Center for Nanointegration Duisburg-Essen (CeNIDE), Universität Duisburg-Essen, Lotharstr. 1, Duisburg D-47048, Germany

[c] EMAT, University of Antwerp, Groenenborgerlaan 171, B-2020 Antwerp, Belgium

## Abstract

Biomedical nanomagnetic carriers are getting a higher impact in therapy and diagnosis schemes while their constraints and prerequisites are more and more successfully confronted. Such particles should possess a well-defined size with minimum agglomeration and they should be synthesized in a facile and reproducible high-yield way together with a controllable response to an applied static or dynamic field tailored for the specific application. Here, we attempt to enhance the heating efficiency in magnetic particle hyperthermia treatment through the proper adjustment of the core–shell morphology in ferrite particles, by controlling exchange and dipolar magnetic interactions at the nanoscale. Thus, core–shell nanoparticles with mutual coupling of magnetically hard ($CoFe_2O_4$) and soft ($MnFe_2O_4$) components are synthesized with facile synthetic controls resulting in uniform size and shell thickness as evidenced by high resolution transmission electron microscopy imaging, excellent crystallinity and size monodispersity. Such a magnetic coupling enables the fine tuning of magnetic anisotropy and magnetic interactions without sparing the good structural, chemical and colloidal stability. Consequently, the magnetic heating efficiency of $CoFe_2O_4$ and $MnFe_2O_4$ core–shell nanoparticles is distinctively different from that of their counterparts, even though all these nanocrystals were synthesized under similar conditions. For better understanding of the AC magnetic hyperthermia response and its correlation with magnetic-origin features we study the effect of the volume ratio of magnetic hard and soft phases in the bimagnetic core–shell nanocrystals. Eventually, such particles may be considered as novel heating carriers that under further biomedical functionalization may become adaptable multifunctional heat-triggered nanoplatforms.

## 1. Introduction

Biomedical nanomagnetics is a truly integrated, multidisciplinary area of research in science since chemistry, materials science, physics, engineering, biology and medicine are incorporated. Recent developments offer exciting possibilities in personalized medicine, with broad applications in imaging, diagnostics and therapy. Biomedical applications require magnetic nanoparticles (MNPs) with several well-defined and reproducible structural, physical, and chemical features. A major goal of such a project is the fine-tuning of the synthesis concluding to

refinement of the magnetic behavior at the nanoscale with emphasis on the relaxation dynamics and surface functionalization of magnetic nanoparticles. The ability of nanotechnology to interact with matter at the molecular scale provides not only the possibility to ascertain the molecular constituents of a disease, but also the way in which these constituents affect the totality of a biological function. The capacity to incorporate an array of structural and chemical functionalities onto the same nanoscale architecture should also enable more accurate, sensitive and precise screening and cure of diseases which appear with significant pathological heterogeneity such as cancer. Despite the fact, that magnetic nanoparticles are attracting considerable and unceasing interest for their biomedical applicability, materials related research projects and clinical practice do not seem to be following fully compatible pathways [1]. In the quest for biomedical nanomagnetic carriers there are several constraints and prerequisites that should be confronted prior to their actual implementation in therapy and/or diagnosis schemes [2]. Starting from the particles themselves, they should first of all possess a well-defined size with minimum agglomeration and they should be synthesized in a facile and reproducible high-yield way. They need to provide a controllable response to an applied static or dynamic field tailored for the specific application. This may be achieved complementarily by tuning magnetic interactions in the collective behavior without sparing the good structural, chemical, colloidal stability under different pH and redox conditions of the biological environment [3]. Obviously, for biomedical applications, nanoparticles should be non-toxic materials or adequately coated to ensure biocompatibility and prevent non-specific reactions with the medium. They should also facilitate the attachment of functional groups for applications based on biological interactions in order to be considered as theranostics platforms [4].

Magnetically induced heat generation from nanoparticles can be used for various purposes initiating from a disease therapy known as hyperthermia. Materials combination and external stimuli (frequency, magnetic field amplitude, gradient direction) allow the proper adjustment of thermal parameters. Hyperthermia is currently regarded as the least-invasive approach in cancer therapy while it may be combined with biomolecular functionalities and offer additional beneficial features such as low dosage due to localization, remote control and on-demand actuation [5]. Moreover, the conversion of electromagnetic energy into heat by nanoparticles can initiate heat-triggered procedures such as drug release and remote control of single cell functions. So far, poor conversion efficiencies have hindered practical applications, since for example drug release and remote control of single cell functions currently require stronger heating conversion efficiency as indicated by AC field application schemes [6] and [7]. Upon exposure to an alternating external magnetic field the magnetic nanoparticles continuously emit heat via relaxation loss (Néel and/or Brown) and/or hysteresis loss pathways depending on their magnetic profile. The specific loss power (SLP), a quantifiable index of the conversion efficiency, has to be maximized by tuning the particle and field features, since it is strongly dependent on size, composition, magnetic profile, field intensity and frequency [8]. The strategy for enhancing SLP is crucial, because higher SLP values result to better efficiency with lower dosage level of nanoparticles and shorter treatment duration. Among the particle features, size and its polydispersity ($s$), saturation magnetization ($M_s$) and magnetic anisotropy ($K_{eff}$) seem to be the key factors to optimize particles' response under external field application [9].

In an attempt to develop novel heat mediators with high thermal energy transfer capability, we have been recently examining the effects of size and composition on the magnetic heating power

of ferrite magnetic nanoparticles ($MFe_2O_4$, M=Fe, Ni, Co, Mn) [10] and [11] and their combinatory approaches as hyperthermia and drug agents [12] and [13]. The choice of ferrite nanoparticles is based on their low inherent toxicity, ease of synthesis, physical and chemical stability and tunable magnetic properties [14]. For instance, $MnFe_2O_4$ is a suitable ingredient as an enhanced MRI contrast agent [1]. On the other hand, $CoFe_2O_4$, is a representative hard material ($K_{eff}=2.0\times10^5$ J/m$^3$) able to generate an exchange coupled nanoscale element with tunable magnetic anisotropy if properly coupled to a representative soft material such as $MnFe_2O_4$ ($K_{eff}=3.0\times10^3$ J/m$^3$). Since the magnetic anisotropy constant $K_{eff}$ is an intrinsic materials property, it is a challenging task to tune anisotropy values of individual nanoparticles as desired. An exchange-coupled nanomagnet by means of interfacial exchange interaction between hard and soft phases has the potential to exhibit tunable magnetism.

Aiming to control nanoscale magnetism, in this manuscript we examine core–shell structures (with a magnetically hard core and magnetically soft shell or vice/versa) encompassing concepts of surface and exchange anisotropy while reflecting morphology and structure effect on the magnetic properties of the nanoparticle [15] and on AC the heating efficacy [16]. Because of the facile synthetic controls that result in nanoparticles with uniform size and shell thickness, excellent crystallinity and size monodispersity, such a magnetic coupling allows for optimal tuning of anisotropy constant $K_{eff}$. Firstly, nanoparticles were synthesized by standard wet chemistry methodologies (i.e. thermal decomposition) that satisfy the requirements of simple and reproducible synthetic protocols with high monodispersity and small size distributions ($s<5\%$). Particles possess tunable magnetic properties approaching bulk values depending on size. Since SLP strongly depends on particle (size, composition and magnetic profile) and field (intensity and frequency) parameters, it was selected as the criterion to monitor-optimize particle performance. Secondly, core–shell magnetic nanoparticles are synthesized, characterized and with the constituent conventional single-phase nanoparticles.

## 2. Experimental procedures

Solutions of magnetic nanoparticle were prepared via standardized wet chemistry methodologies [17] based on the thermal decomposition of molecular precursors. The reagents manganese(II)-acetate tetrahydrate, cobalt(II)-acetate tetrahydrate, iron(III)-acetylacetonate, oleic acid (technical grade 90%), and octadecene (technical grade 90%) were purchased from Aldrich, ethanol absolute and acetone absolute from VWR, toluene from Merck and tetrahydrofuran (THF) from Riedel-de-Haen. Table 1 lists the samples, the relevant ingredients and quantities used for their synthesis. Samples S1 and S2 are Mn and Co ferrite single-phase magnetic nanoparticles, respectively. These first two reference samples (S1–S2) were synthesized by dissolving the proper precursors (Fe(acac)$_3$ and either Mn(CH$_3$COO)$_2$ for S$_1$ or Co(CH$_3$COO)$_2$ for S$_2$) together with oleic acid acting as a surfactant. At the second stage, the synthesized S1, S2 MNPs were also used as seed materials to form core–shell nanoparticles and to check the intermixing efficiency in the synthetic processes of the bimagnetic ferrite samples (S3 and S4). In more detail, for the sample S3 (core–shell nanoparticles) the $MnFe_2O_4$ synthetic procedure of sample S1 was repeated together after the addition of 78 mg dried $CoFe_2O_4$-particles to act as cores for the core–shell morphology where $MnFe_2O_4$ would be the shell and oleic acid, oleyamine and tetraoctylamine were employed as surfactants. Analogously, for sample S4 (core–shell nanoparticles), the $CoFe_2O_4$ (S2) synthetic procedure was repeated with the addition of

78 mg dried $MnFe_2O_4$ particles to serve as seeds (cores), $CoFe_2O_4$ would form the shell and oleic acid, oleyamine were employed as surfactants.

Table 1. Notation of samples, parameters and deliverables of wet chemistry methodology.

| Sample | Ingredients and quantities | Magnetic Nanoparticles |
|---|---|---|
| S1 | 2 mmol $Mn(CH_3COO)_2$, 4 mmol $Fe(acac)_3$, 18 mmol oleic acid | $MnFe_2O_4$ |
| S2 | 2 mmol $Co(CH_3COO)_2$, 4 mmol $Fe(acac)_3$, 18 mmol oleic acid | $CoFe_2O_4$ |
| S3 | 78 mg dried $CoFe_2O_4$-particles, 1 mmol $Mn(CH_3COO)_2$, 2 mmol $Fe(acac)_3$, 9 mmol oleic acid and 9 mmol oleylamine | shell: $MnFe_2O_4$ core: $CoFe_2O_4$ |
| S4 | 78 mg dried $MnFe_2O_4$-particles, 1 mmol $Co(CH_3COO)_2$, 2 mmol $Fe(acac)_3$, 9 mmol oleic acid, 4.5 mmol oleylamine, 4.5 mmol tetraoctylamine | shell: $CoFe_2O_4$ core: $MnFe_2O_4$ |

In all cases, the corresponding mixture was injected into 30 mL octadecene placed in a spherical flask and heated up to 300 °C without a reflux-condenser to evaporate side-products and then heating continued to reach 320 °C (boiling point) and allow reflux for 30 min after adapting a condenser. A first fraction of particles was separated by a permanent magnet, dispersed in ethanol by ultrasonification, separated again magnetically and finally dispersed in toluene or THF. The remaining particles were destabilized by the addition of excess ethanol, separated by centrifugation (6k–14k rpm, depending on particle size), and re-dispersed in toluene or THF. This procedure was repeated 2 times. After the general procedure, the THF dispersion was moderately destabilized by addition of 1/3 volume 1-propanol, after which the larger particles could be separated by a magnet while the smaller particles remained in solution.

The structural and morphological properties and the composition of the deposited particles were investigated ex-situ by high resolution and scanning transmission electron microscopy (HRTEM and STEM); the latter combined with energy dispersive X-ray spectroscopy (EDXS). We used a double Cs-corrected JEOL JEM-2200FS microscope operated at 120 kV, for conventional TEM imaging. For HRTEM we used a Philips Tecnai F20 Supertwin microscope and a FEI Tecnai G2, both operated at 200 kV and equipped with field emission guns and Si(Li) EDX detectors. Samples suitable for STEM were prepared by drop casting the aqueous solution of the nanoparticles on holey, carbon-coated copper grids. STEM-EELS measurements were performed using a double aberration corrected 'Cubed' FEI Titan microscope operated at 300 kV. The EELS spectra were analyzed using Digital Micrograph software. PCA treatment of the large set of spectral data was employed to suppress the uncorrelated noise [18], [19] and [20]. The magnetic properties signified by hysteresis and standard zero-field cooled (ZFC)–field-cooled (FC) curves (followed by field-heat (FH) curves: an additional sequence recorded as the last stage of a typical ZFC–FC sequence) were recorded by a Quantum Design MPMS SQUID magnetometer within a field range of ±5 T and a temperature range of 5–300 K.

Next, the heating efficiency at varying solution concentrations (0.5–4.0 mg/mL) were measured in an AC magnetic field at $f$=765 kHz and field amplitudes of $H_{ac}$=20–28 kA/m. It should be mentioned here that despite the use of a relatively high frequency (765 kHz) leading to a rather high $Hf$ product [21] ($\sim 2 \times 10^{10}$ Am$^{-1}$ s$^{-1} \gg \sim 5 \times 10^{8}$ Am$^{-1}$ s$^{-1}$ which is the estimated threshold for major discomfort), analogous protocols are currently examined (also in-vitro) as alternatives to overcome the usual constraints of limited heating efficacy [2] and [3].

The solution was placed in the center of a water cooled induction coil of 23 mm diameter consisting of three turns and connected to an AC field generator of 4.5 kW. During measurement, heating and natural cooling sequences were recorded, each of them, for about 600 s. The hyperthermia efficacy was quantified by estimating the specific loss power (SLP), defined as $SLP = \frac{W}{m_m} = \frac{\Delta Q}{\Delta t\, m_m} = C_p \frac{m_f}{m_m} \frac{\Delta T}{\Delta t}$ which refers to the amount of energy converted into heat ($W$) per time ($\Delta t$) and mass of the magnetic material ($m_m$) where $Cp$ is the specific heat of the solution, $m_f$ the solution mass and $\Delta T/\Delta t$ the initial slope of the heating curve in a magnetic field, extracted from experimental data, before the interference of heat conduction becomes significant [22]. In order to extract a more accurate $SLP$ value, the reference signal corresponding to the solvent was subtracted from the measured data, while the thermal losses to the environment were also considered in the $SLP$ estimation [23].

## 3. Results and discussion

Our reference nanocrystals are shown in Fig. 1 where the TEM images confirm single phase nanoparticles $MnFe_2O_4$ (S1-top row) and $CoFe_2O_4$ (S2-bottom row). The MNPs show a high degree of monodispersity with a narrow size distribution of $s$<10% depicted at the right side ( Fig. 1c and f). The average size of the synthesized nanoparticles is 10.0 nm and 15.0 nm for $MnFe_2O_4$ and $CoFe_2O_4$ respectively. The electron diffraction patterns appear as insets in the low magnification images ( Fig. 1a and d) and confirm the spinel ferrite structure in both cases. The continuous atomic lattice fringes in the high resolution TEM (HRTEM) images ( Fig. 1b and e) indicate that the nanocrystals are highly crystalline single crystals as also indicated by the FFT insets.
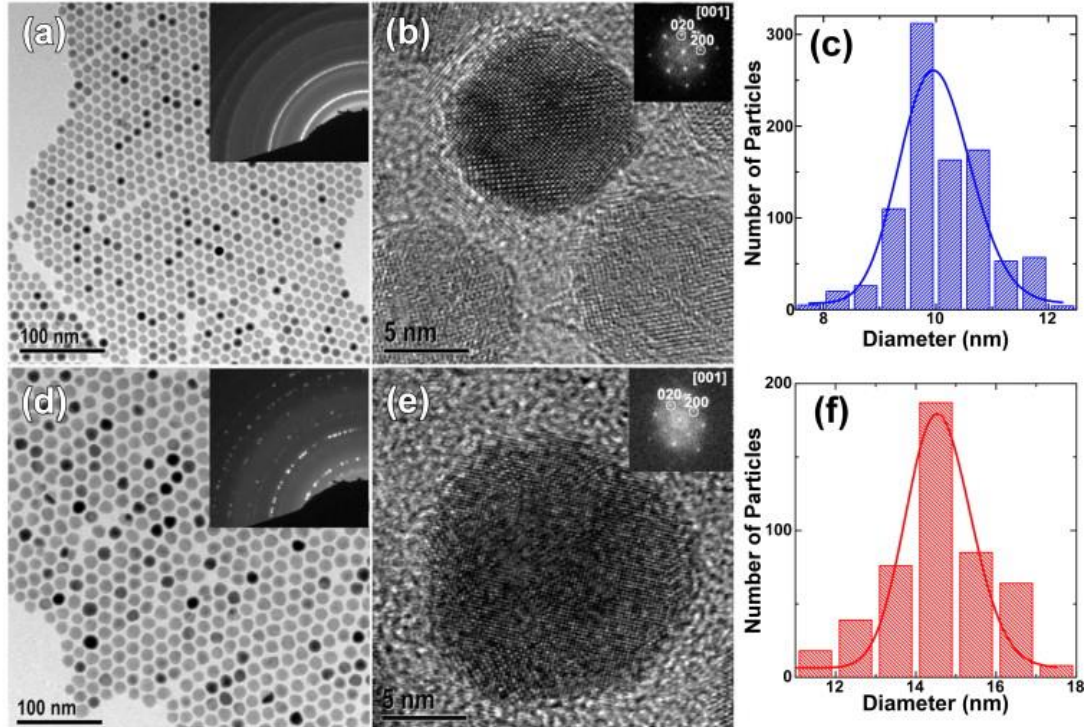
Fig. 1. Bright-field TEM imaging of S1: $MnFe_2O_4$ (top row) and S2: $CoFe_2O_4$ (bottom row) nanoparticles. (a), (d) low magnification images with corresponding electron diffraction patterns as insets confirming the presence of the $MnFe_2O_4$ and $CoFe_2O_4$ respectively (b), (e) HRTEM images of S1: $MnFe_2O_4$ and S2: $CoFe_2O_4$ respectively and (c), (f) corresponding size distributions.

In Fig. 2 an overview of SQUID magnetometry experiments for samples S1 and S2 is shown. Fig. 2a depicts hysteresis loops at high (300 K) and low (5 K) temperatures where $CoFe_2O_4$ (S2) particles yield saturation magnetization and coercivity approximating typical hard ferrite bulk-phase behavior [24]. Contrary, the S1 sample comprising of $MnFe_2O_4$ smaller sized nanoparticles does not follow the typical behavior of the soft ferrite and seems unable to complete saturation under the experimental conditions. This is attributed to the superparamagnetism of nanoparticles at room temperature lacking saturation and coercivity as a result of the combination of the small size (10 nm) and the soft magnetic character. This is also supported by divergence of the ZFC–FC branches indicating a blocking temperature at 100 K as shown in Fig. 2b. Below this temperature, nanoparticles become ferrimagnetic and thus coercivity arises as shown by the 5 K hysteresis loop. Sample S2 maintains ferrimagnetic features up to 300 K since ZFC and FC branches separate above this temperature. The bulk-like behavior is also evidenced by the difference in the FH which may be attributed to the magnetic annealing effect observed in solid solutions of cobalt ferrite and iron ferrite (called cobalt-substituted magnetite) and in some other mixed ferrites containing cobalt [24].
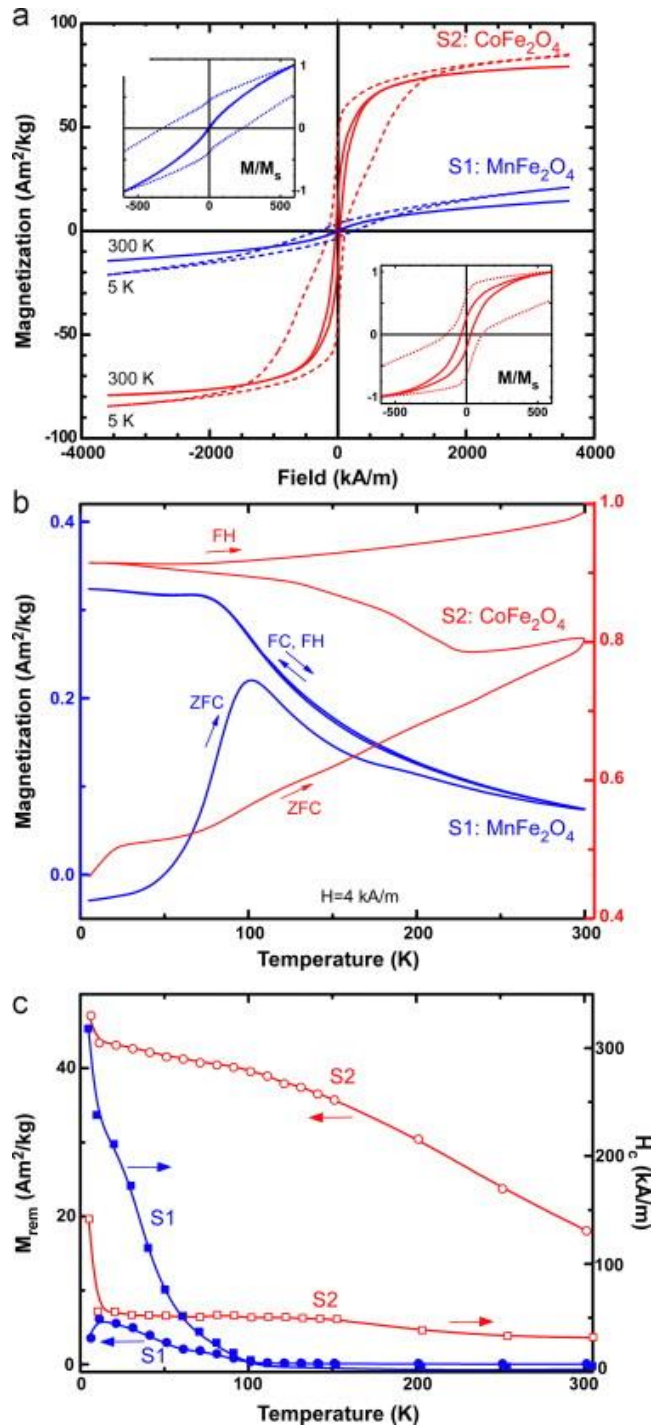
Fig. 2. SQUID magnetometry characterization of the S1: $MnFe_2O_4$ and S2: $CoFe_2O_4$ nanoparticles. Hysteresis loops at 5 and 300 K. Insets: detail of loops (normalized against magnetization value at maximum applied field) at low fields showing coercivity evolution (a). ZFC–FC–FH sequence under 4 kA/m (b). Temperature dependence of remanent magnetization and coercivity (c).

This means heat treatment in a magnetic field, sometimes called a thermomagnetic treatment inducing anisotropy. The effect depends on, but is not caused by, the presence of metal-ion

vacancies in the lattice created by heating the ferrite in oxygen during the SQUID sequence. It follows that a material that responds to magnetic annealing will undergo local self-magnetic-annealing if it is heated, in the demagnetized state and in the absence of a field, to a temperature where substantial diffusion is possible. The remanent magnetization and coercivity values within the temperature range of 5–300 K as estimated from the corresponding hysteresis loops are shown in Fig. 2c, where for sample S1 values diminish above blocking temperature indicative of superparamagnetic transition, while sample S2 follows a gradual decrease with temperature usually followed by ferro(i)magnetic materials. Such a feature exhibited in FH curves is usually met in ferro(i)magnetic systems where their magnetic history is a crucial factor, thus further supports the distinction between superparamagnetic (S1) and ferrimagnetic (S2) samples.

As anticipated from the synthetic sequence followed, samples S3 and S4 should yield a core–shell structure with a core size of 15 nm $CoFe_2O_4$ (20% of the total volume) and 10 nm $MnFe_2O_4$ (25% of the total volume) and shell thickness of ~6 ($MnFe_2O_4$) and 4 nm ($CoFe_2O_4$) respectively since S1 and S2 ferrite nanoparticles were used as seed-ingredients in the synthesis procedure.

The lack of image contrast difference between the core and the shell in the bright-field TEM images (Fig. 3a and d) arises from the small difference in scattering strength between Mn and Co and also from the consequent epitaxial overcoating of the respective cores by the shell of $CoFe_2O_4$ or $MnFe_2O_4$ due to a negligible lattice mismatch. By direct comparison of the images, it seems that the spherical homogeneity is favored in cases where the core material is $MnFe_2O_4$ and the overall particle size is smaller (Fig. 3c and f). Selected area electron diffraction patterns (insets in low magnification images Fig. 3a and d) are confirmative of the coexistence of both phases. The highly crystalline order of the nanocrystals is revealed in the HRTEM images (Fig. 3b and e) and their FFT images shown as insets. Although, we cannot distinguish the different phases in the nanoparticles either by analyzing the SAED or the HRTEM images and their FFTs since $MnFe_2O_4$ and $CoFe_2O_4$ have the same crystallographic structure, we found a good match of the structure with the tetragonal phase of $MnFe_2O_4$ (PDF#38-430), from the analysis of series of HRTEM images.
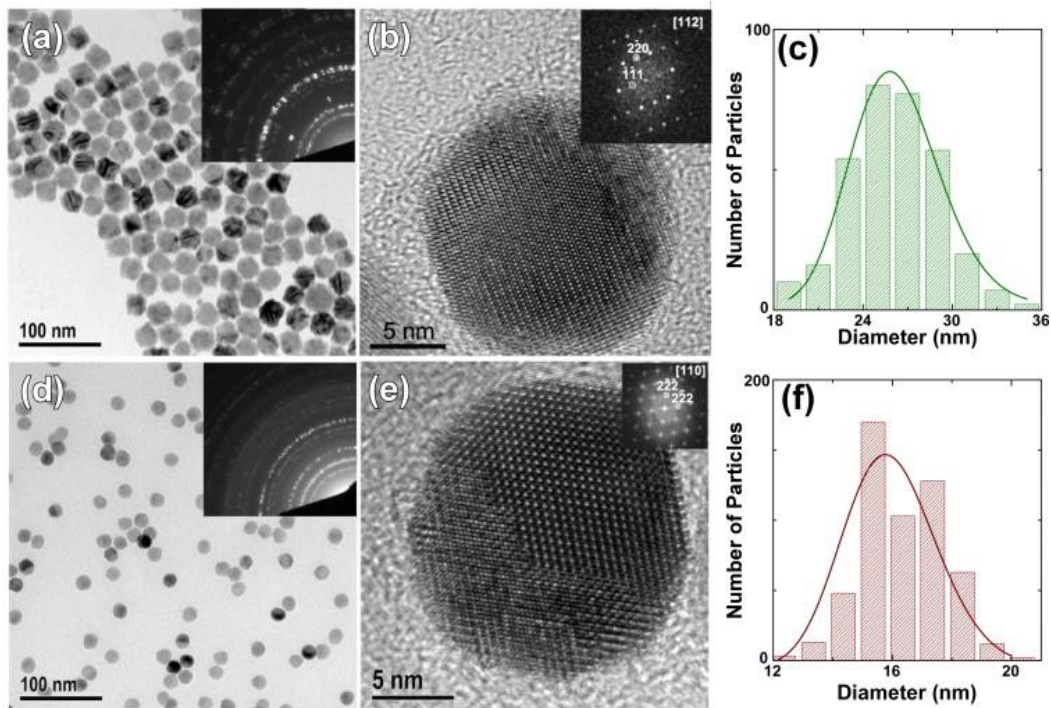
Fig. 3. S3 (top row) and S4 (bottom row) bimagnetic core–shell ferrite samples. (a), (d) bright-field TEM images with EDPs as insets. (b), (e) HRTEM images of individual particles based on FFT analysis as shown in the corresponding insets. (c), (f) size distribution and log–normal fitting curve for bimagnetic core–shell ferrite samples.

Since TEM imaging does not provide clear evidence of the core–shell morphology, in order to verify the formation of the core–shell architecture, EDXS and EELS were used to analyze the chemical composition and illustrate the core/shell morphology. In EDXS when the electron beam passed through the center of an individual nanocrystal, all elements of Mn, Fe, Co, and O from both the core and the shell showed up in Fig. 4 for samples S3 and S4, while in case of pure ferrite samples (S1 and S2) either Mn or Co were alternatively detected together with Fe and O. The Cu signal present in all spectra derives from Cu TEM grid. Subsequently, EELS mapping and corresponding analysis were carried out. In Fig. 5 EELS maps of the sample S4 with a $CoFe_2O_4$ shell and a $MnFe_2O_4$ shell sample are presented, from the area which is shown in Fig. 5a, in which Fe, Mn and Co are color-coded green, red and blue, respectively. Fe is distributed uniformly throughout the nanoparticles, Co is partially located on nanoparticle surface region while Mn is located mostly in the central nanoparticle region. We have the formation of a a core–shell structure, where Fe, Co and Mn exist at the core location while only Fe and Mn are found on the shell region.
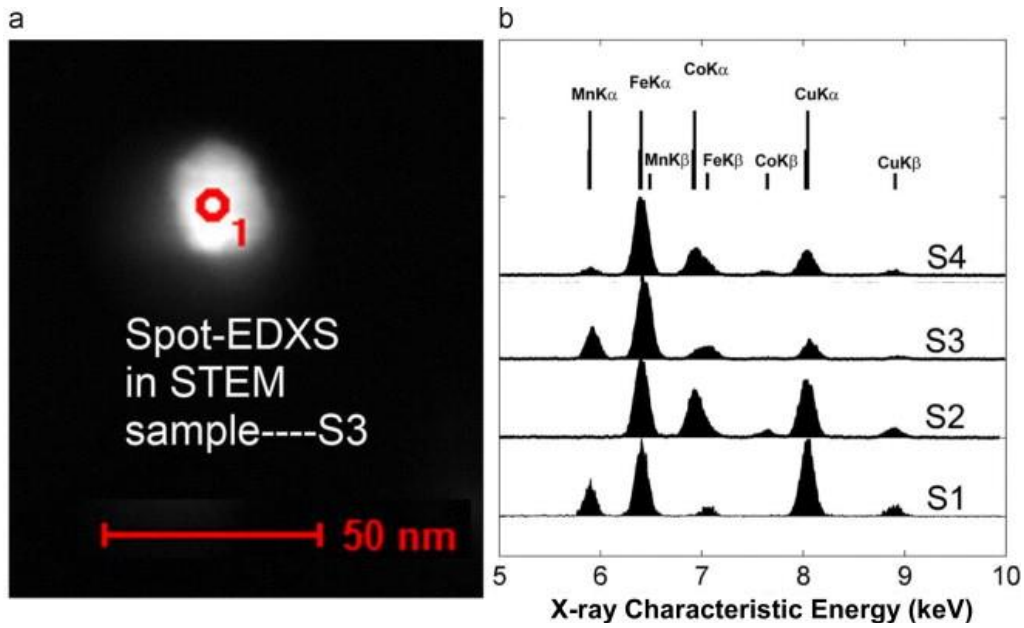
Fig. 4. (a) Representative image indicating Spot-EDXS experiment in STEM mode for sample S3 (with a $MnFe_2O_4$ shell and a $CoFe_2O_4$ core). (b): EDX spectra for all samples under study (S1–S4) indicating elemental composition.
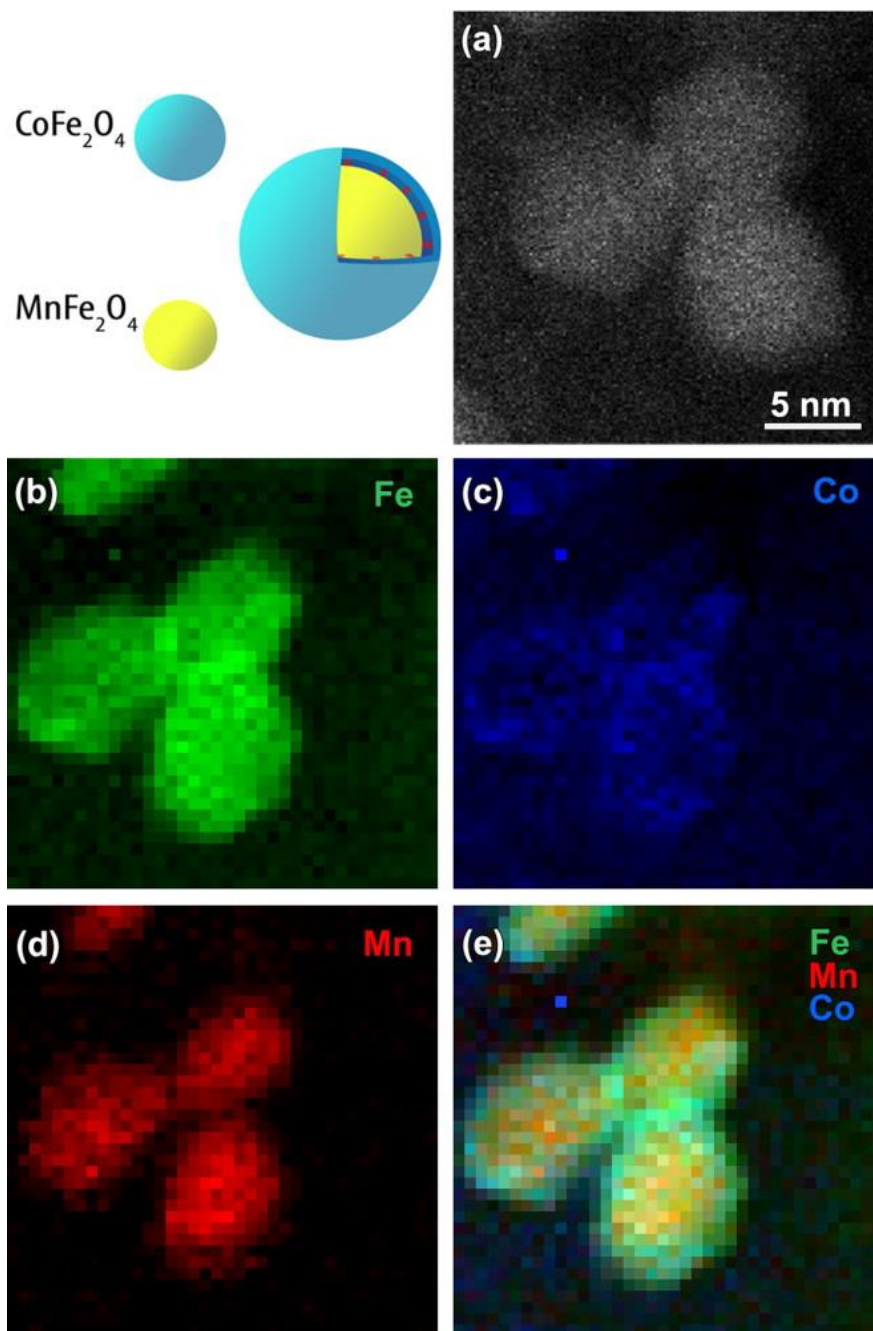
Fig. 5. S4 sample with a $CoFe_2O_4$ shell and a $MnFe_2O_4$ core (a) schematic representation, (b) HAADF-STEM image of the particles which was used for the acquisition of the EELLS maps (b) Fe map, (c) Co map, (d) Mn map and (e) color map with Fe (green) Co (blue) and Mn (red). (For interpretation of the references to color in this figure legend, the reader is referred to the web version of this article.)

A further confirmation of the core−shell architecture was evidenced by the magnetic features comparison collected in Fig. 6. From Fig. 6a, there is direct evidence that bimagnetic systems are completely different from their counterparts, since hysteresis appears much enhanced even when compared with the hard ferrite sample S2.
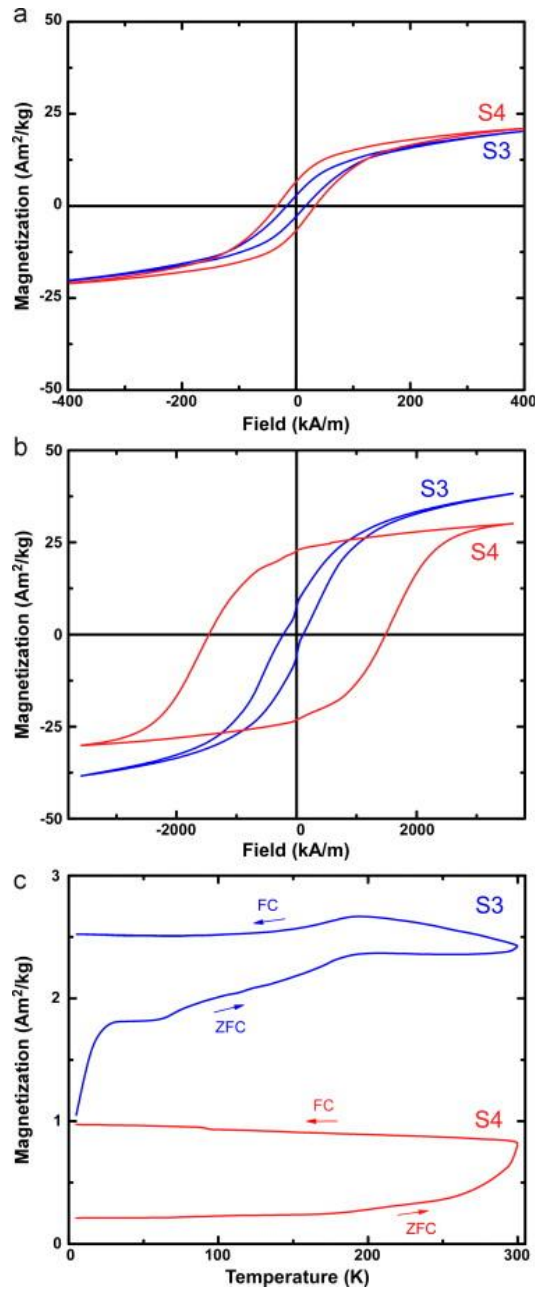
Fig. 6. Comparison of magnetic features in samples of core–shell ferrites (S3 with shell of $MnFe_2O_4$ and a core of $CoFe_2O_4$, S4 with shell of $CoFe_2O_4$ and a core of $MnFe_2O_4$). Magnetic hysteresis loops at 300 (a), 5 K (b) and ZFC–FC curves under 4 kA/m (c).

This observation implies some type of magnetic interaction between the two phases, thus the existence of a core–shell structure may be anticipated in agreement with relevant studies [25]. The effect becomes more pronounced in the low temperature (5 K) hysteresis loops (Fig. 6b) where substantial coercivity arises due to the tunable coupling between the two phases. The success level for exchange coupling is depicted not only by coercivity magnitude but also by the kinks of the loops as expected by the coexistence of two substantially different coercive fields within the same nanoparticle entity [26]. Similar kinks are also observed in the ZFC–FC curves showing the co-existence of two phases, though separated below 300 K, yet differences appear

also in branch tendencies outlining the role of exchange coupling intensity due to inhomogeneous magnetization states at interfaces [15]. In sample S4 the exchange coupling seems to be better tuned, since a more uniform hysteresis loop and ZFC–FC behavior is exhibited. This is indicative of a harder phase not directly arising from the natural mixing of two phases but from the occurrence of exchange coupling which explains the significant coercivity increase [15] and [16].

A summary of structural and magnetic scores is collected in Table 2. The numbers in brackets next to room temperature coercivity correspond to values estimated from the simplified equation $H_c=H_H(1-f_s)$ based on the assumption that there is a distinct difference between the anisotropy constants and saturation magnetization between the constituent hard and soft phases [26]. $H_H$ is the coercivity of the hard phase ($CoFe_2O_4$) and $f_s$ its volume fraction. The relative volume fraction of the hard phase lowers the saturation magnetization (since smaller $MnFe_2O_4$ content exists compared to S4) and the coercivity enhances governed by the hard phase component.

Table 2. Structural and magnetic features overview of samples of pure and bimagnetic core–shell ferrites.

| Sample | Size (nm) ($\pm7-12\%$) | EDX-HRTEM ($\pm 2\%$) | | | $M_{rem}(A\ m^2/kg)$ 300 K | $H_c(kA/m)$ 300 K | $M_s(A\ m^2/kg)$ 300 K |
|---|---|---|---|---|---|---|---|
| | | Mn | Co | Fe | | | |
| S1 (0%)[a] | 10.0 | 30 | 0 | 70 | 0 | 0 (0) | 14.5 |
| S2 (100%)[a] | 15.0 | 0 | 37 | 63 | 18.3 (59%)[b] | 31 (31)[c] | 79.2 |
| S3 (20%)[a] | 26.0 | 22 | 8 | 70 | 3.2(10%)[b] | 17 (20)[c] | 33.3 |
| S4 (75%)[a] | 16.0 | 8 | 21 | 71 | 7.5(29%)[b] | 28 (26)[c] | 26.4 |

a $CoFe_2O_4$ within the nanoparticle volume.
b $M_{rem}/M_s$ ratio.
c Values estimated from the equation $H_c=H_H(1-f_s)$.

In Fig. 7 an overview of magnetic particle hyperthermia results is depicted. The temperature difference during AC magnetic particle hyperthermia (Fig. 7a) and the corresponding SLP values (Fig. 7b) at particle concentrations from 0.5 to 4 mg/mL for samples S1–S3 indicate the superior behavior of sample S3 resulting from coexistence of two phases. The negative tendency of hyperthermia scores with increasing concentration arises from the ferrimagnetic character of samples since the denser the colloid, the stronger the dipolar interaction resulting to the less effective the AC magnetic field in MNPs manipulation as we discussed in detail in a previous work [27]. Since we wanted to compare sample efficacies under identical and realistic conditions we have chosen the concentration of 1 mg/mL for further study of all samples as the prerequisite of hyperthermia bottom threshold ($\Delta\theta{\geq}4$) is approached or even surpassed while SLP values are maintained at reasonably high levels. In Fig. 7c a complete series of AC hyperthermia curves is shown for all samples under identical conditions (1 mg/mL, 28 kA/m, 765 kHz) where shaded

band denotes the desirable hyperthermia levels (41–45 °C) for a successful treatment. It appears that both bimagnetic core–shell particles yield superior heating efficacies, though it seems more appropriate to use $MnFe_2O_4$ as core (as in sample S4 probably due to its smaller core size: 10 nm) as it results to better structural and morphological features (as discussed in Fig. 3), providing higher quality interfaces between the hard and the soft phase.
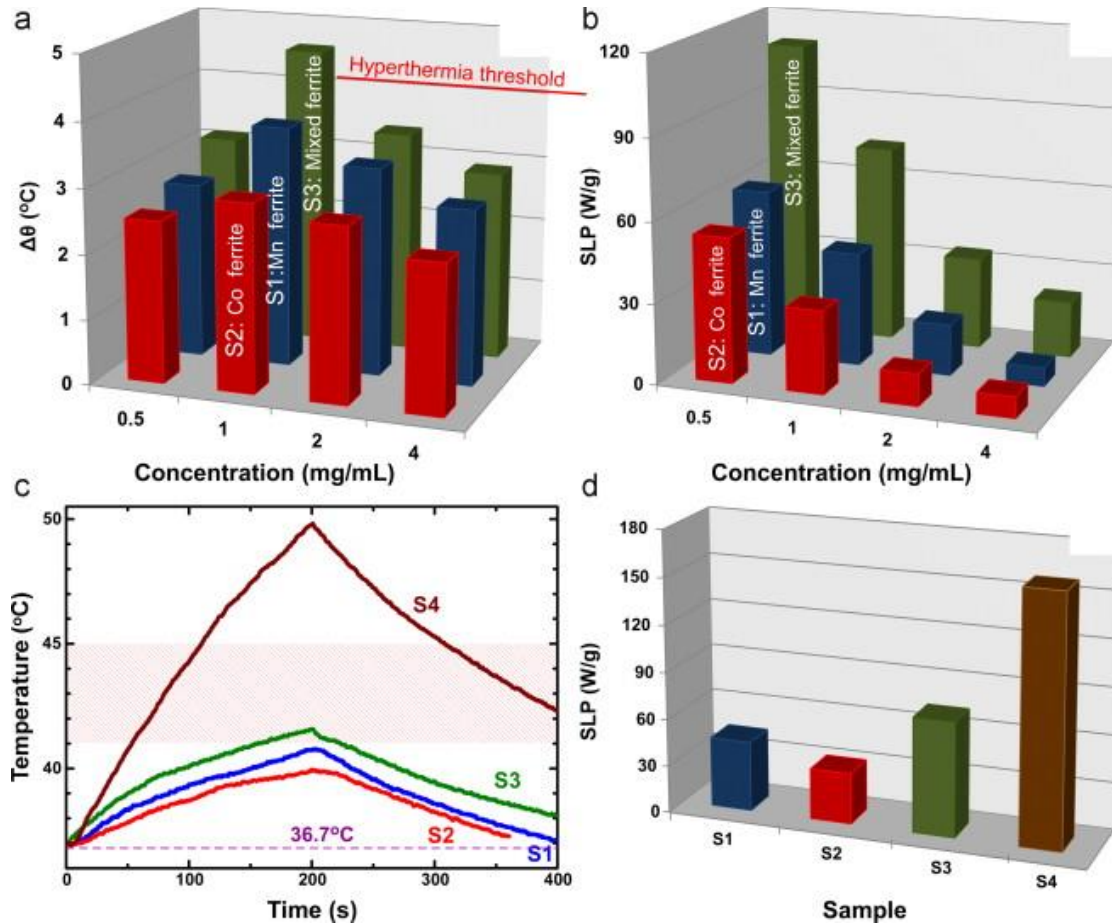


Fig. 7. Concentration influence on AC (28 kA/m, 765 kHz) magnetic hyperthermia parameters (a) temperature rise and (b) SLP values for samples S1–S3. Comparison of heating efficiency between pure and bimagnetic core–shell ferrites: (c) Experimental magnetic hyperthermia cycles for samples S1–S4 of similar conditions $c$=1 mg/mL, 28 kA/m, 765 kHz. Shaded band denotes efficient hyperthermia levels (d) corresponding SLP values (±10%) indicating superior efficiency of bimagnetic core–shell ferrites (S3 and S4) vs pure ferrites (S1 and S2).

As Fig. 7d shows, the tunable magnetic features exhibited by the bimagnetic core-shell particles seem to have a direct influence on SLP values (from 73 for S3 to 160 W/g for S4), though SLP records of samples under study are rather small when compared with relevant studies [14], [15] and [16]. This may have to do with the quality of the interface between the hard and the soft phase tuning the exchange coupling intensity. When the soft and hard magnetic phases are coupled, soft phase becomes rigidly pinned by hard phase at the interface. The flatness of the interface between the soft and the hard phase is critical to enhance the exchange interactions between magnetic spins. Another potential reason for the limited increase of heating efficiency is the multitude of parameters affecting SLP. The SLP is size dependent and in the

superparamagnetic regime (sizes<~20 nm) is mainly governed by intrinsic particle properties [27]. As particles grow in size, they tend to become ferrimagnetism where the amount of dissipated heat is gradually turning to be proportional to the area of the hysteresis loop [10]. In such a case SLP values may be further optimized by contributions directly affecting the hysteresis loop features (i.e. the fingerprint of ferrimagnetism) via anisotropy tuning of core-shell morphology. However, since in our case, core and MNPs sizes yield relatively small values (<30 nm), intrinsic particle features are still important, hindering interactions (exchange or dipolar) from further enhancing SLP values. As the small values of $M_{rem}/M_s$ ratio ( Table 2) indicate, the squareness inclination of the hysteresis loop providing the fractional estimate of the maximum energy product does not seem adequate for exchange coupling by Stoner−Wohlfarth model [15]. Another interesting aspect arises from the direct correlation of the maximum AC hyperthermia field of 28 kA/m and the coercive field (and consequently with the anisotropy field) of the nanoparticles exposed to it as recently discussed [28]. If $H_{max} \gg H_c$ then the hysteresis loop is fully saturated yielding maximum heating efficiency. On the other hand, if $H_{max} \sim H_c$ or even $H_{max} < H_c$ then only minor loops are cycled, thus, resulting to smaller heating efficiency. An estimation of product of $M_s H_c$ (assumption of a square loop) at 300 K provides an indication of the maximum energy product that may be achieved by the corresponding particles provided $H_{max}$ is big enough to overrule the $H_c$. As shown in Table 2 sample S2 is at optimum conditions, thus, its SLP value may not be substantially enhanced. However, for the bimagnetic core-shell samples (S3 and S4) SLP scores, appearing enhanced though in a limited way, outline the role of exchange anisotropy and may further optimized if $M_{rem}$ together with $M_s$ and $H_c$ are increased by adequately tuning of exchange coupling of core−shell components. It seems feasible that, if size regimes of both core and shell are properly adjusted, anisotropy optimization may also occur resulting in further enhancement of SLP efficacy.

## 4. Conclusions

In this work, we examined the effect of incorporating core−shell morphologies as an alternative approach in enhancing AC magnetic particle hyperthermia efficacy via nanomagnetism tuning. Initially, we studied pure ($MnFe_2O_4$ and $CoFe_2O_4$) ferrite particles and then attempted to synthesize bimagnetic core−shell particles with a seed-mediated growth where initial nanoparticles were used as substrates. The use of core−shell bimagnetic morphology instead of careful control of size and homogeneity in single phase particles seems to address the issue of enhanced hyperthermia agents more successfully since bimagnetic particles exhibit scores one order of magnitude higher that initial materials. Thus, we surmise that by more delicate tuning between core and shell materials and thicknesses further simultaneous optimization of $M_s$, $M_{rem}$, $H_c$ and $K$ may be achieved. The idea of incorporating a bimagnetic structure than surveying individual materials seems to provide a more effective pathway towards enhanced hyperthermia agents via nanomagnetism tuning.

## References

[1] D. Yoo, J.-H. Lee, T.-H. Shin, J. Cheon,Acc. Chem. Res., 44 (2011), p. 863

[2] B. Kozissnik, A.C. Bohorquez, J. Dosbon, C. Rinaldi, Int. J. Hyperth., 29 (8) (2013), pp. 706–714

[3] G. Salas, S. Veintemillas-Verdaguer, M. del Puerto Morales, Int. J. Hyperth., 29 (8) (2013), pp. 768–776

[4] C. Grüttner, K. Müller, J. Teller, F. Westphal, Int. J. Hyperth., 29 (8) (2013), pp. 777–789

[5] Q.A. Pankhurst, N.K.T. Thanh, S.K. Jones, J. Dobson, J. Phys. D: Appl. Phys., 42 (2009), p. 224001

[6] C.S.S.R. Kumar, F. Mohammad, Adv. Drug Deliv. Rev., 63 (2011), p. 789

[7] E.A. Vitol, V. Novosad, E.A. Rozhkova, Nanomedicine, 7 (10) (2012), pp. 1611–1624

[8] S. Dutz, R. Hergt, Int. J. Hyperth., 29 (8) (2013), pp. 790–800

[9] K. Krishnan, IEEE Trans. Magn., 46 (2010), p. 2523

[10] K.D. Bakoglidis, K. Simeonidis, D. Sakellari, G. Stefanou, M. Angelakeris, IEEE Trans. Magn., 48 (NO. 4) (2012), p. 1320

[11] K. Vamvakidis, D. Sakellari, M. Angelakeris, C. Dendrinou-Samara, J. Nanopart. Res., 15 (2013), p. 1743

[12] M. Filippousi, S.A. Papadimitriou, D.N. Bikiaris, E. Pavlidou, M. Angelakeris, D. Zamboulis, H. Tian, G. Van Tendeloo, Int. J. Pharm., 448 (2013), pp. 221–230

[13] M. Filippousi, T. Altantzis, G. Stefanou, M. Betsiou, D.N. Bikiaris, M. Angelakeris, E. Pavlidou, D. Zamboulis, G. Van Tendeloo, RSC Adv., 3 (2013), p. 24367

[14] I. Sharifi, H. Shokrollahi, S. Amiri, J. Magn. Magn. Mater., 324 (2012), pp. 903–915

[15] S.-H. Noh, W. Na, J.-T. Jang, J.-H. Lee, E.J. Lee, S.H. Moon, Y. Lim, J.-S. Shin, J. Cheon

Nano Lett., 12 (7) (2012), pp. 3716–3721

[16] J.H. Lee, J.T. Jang, J.S. Choi, S.H. Moon, S.H. Noh, J.W. Kim, J.G. Kim, I.S. Kim, K.I. Park, J. Cheon, Nat. Nanotechnol., 6 (2011), pp. 418–422

[17] C. Pereira, A.M. Pereira, C. Fernandes, M. Rocha, R. Mendesm, M.P. Fernandey-Garcia, A. Guedes, P.B. Tavares, J.-M. Greneche, J.P. Araujo, C. Freire, Chem. Mater., 24 (2012), p. 1496

[18] I. Jolliffe, Principal Component Analysis, (second ed.)Springer, New York (2002)

[19] M. Bosman, M. Watanabe, D.T.L. Alexander, V.J. Keast, Ultramicroscopy, 106 (2006), p. 1024

[20] S. Lichtert, J. Verbeeck, Ultramicroscopy, 125 (2012), p. 3542

[21] S.E. Barry, Int. J. Hyperth., 24 (2008), pp. 451–466

[22] H. Mamiya, B. Jeyadevan, J. Magn. Magn. Mater., 323 (2011), p. 1417

[23] K. Simeonidis, C. Martinez-Boubeta, Ll Balcells, C. Monty, G. Stavropoulos, M. Mitrakas, A. Matsakidou, G. Vourlias, M. Angelakeris, J. Appl. Phys., 114 (2013), p. 103904

[24] B.D. Cullity, C.D. Graham, Introduction to Magnetic Materials (second ed.)John Wiley & Sons, Inc., Hoboken, New Jersey (2009)

[25] Q. Song, Z. John Zhang, J. Am. Chem. Soc., 134 (24) (2012), pp. 10182–10190

[26] J. Carrey, B. Mehdaoui, M. Respaud, J. Appl. Phys., 109 (2011), p. 083921

[27] D. Serantes, D. Baldomir, C. Martinez-Boubeta, K. Simeonidis, M. Angelakeris, E. Natividad, M. Castro, D.-X. Chen, A. Sanchez, Ll Balcells, B. Martínez, J. Appl. Phys., 108 (2011), p. 073918

[28] D. Serantes, K. Simeonidis, M. Angelakeris, O. Chubykalo-Fesenko, M. Marciello, M. Morales, D. Baldomir, C. Martinez-Boubeta, J. Phys. Chem. C, 118 (2014), pp. 5927–5934